Electronic Supplementary Information

Spin-orbital regulation of Iron-nitrogen sites in phthalocyanine catalysts for ultrahigh energy efficiency Zn–Air/Iodide hybrid batteries

Xue Liu, Miao Wang, Dongyang Xie, Hongyan Zhuo, Wenmiao Chen,* Yuexing Zhang,* Yanli Chen*

1.Experimental section

1.1 Chemical and reagents

All chemical reagents are of analytical grade purity and are used directly without further purification.

1.2 Characterization

Laboratory powder X-ray diffraction patterns were collected for the samples on a Rigaku Ultima IV X-ray diffractometer with Cu Kα source (40 kV, 40 mA). The morphology and struct. of the samples were observed on field-emission scanning electron microscope (SEM, Quant 250FEG) equipped with energy-dispersive X-ray (EDX) detector and high-resolution transmission electron microscopy at an acceleration voltage of 200 kV (TEM, JEM-2100F). Raman scattering spectra were recorded on a laser Raman microscope system (Nanophoton RAMANtouch) with an excitation wavelength of 532 nm. X-ray photoelectron spectroscopic (XPS) meas.ments were conducted on an Axis Ultra instrument from Kratos using monochromatic Al Kα radiation. Micromeritics Belsorp-max analyzer was applied to meas. the Brunauer Emmett Teller (BET) surface area and pore size distribution (PSD). The XAFS spectra at Fe K-edge were acquired at 4B9A station in Beijing Synchrotron Radiation Facility (BSRF, operated at 2.5 GeV with a maximum current of 250 mA). The raw EXAFS data acquired were then background-subtracted, normalized, and Fourier-transformed by using the ATHENA program in the IFEFFIT software package. Least-squares curve parameter fitting was performed using the ARTEMIS module of IFEFFIT software packages. The Fe K-edge XANES data were recorded in a fluorescence mode. Fe foil was used as references.

1.3 Electrochemical meas.ments

The rotary disk electrode (RDE, Pine Research Instrumentation, Inc.) with a Pine Modulated Speed Rotator (Pine Research Instrumentation, Inc.) meas.ments described in this study was used to meas. cyclic voltammetry (CV) and LSV. The electrocatalytic activity of all catalysts for oxygen reduction was studied in 0.1 M aq. KOH solution in an oxygen saturated condition using a rotating ring-disk electrode (RRDE, Pine Research Instrumentation, Inc.) at a rotation speed of 1600 rpm. All the electrochemical meas.ments were meas.d by the aid of a CHI 760E electrochemical analyzer in a three-electrode electrochemical cell at room temperat. (*ca*. 25℃). The glassy carbon rotating

disk (GC, 5.0 mm in diameter) modified with various electrocatalysts and silver/silver chloride (Ag/AgCl, in saturated KCl saturated solution) were used as the working and reference electrodes, respectively. For ORR, platinum foil and graphite rod served as the auxiliary electrode in alkaline medium. All potentials of the working electrode were converted *versus* reversible hydrogen electrode (RHE) using the following equation:

$$E_{(RHE)} = E_{Ag/AgCl} + 0.0592\ pH + E^{\Theta}_{Ag/AgCl}$$

where $E^{\Theta}_{Ag/AgCl}$ is 0.1989 V.

In a typical proced., the GC electrode in both cases was prepared by mixing 5.0 mg of as-prepared samples in 0.8 mL of an isopropyl alcohol solution containing 30 μL of a 5 wt% Nafion solution and then ultrasonicated for 30 min to form a homogeneous slurry. Then 10 μL of ink was pipetted onto a polished GC electrode surface and dried naturally to form a homogeneous membrane. The general loading of the electrocatalysts on the working electrode is 0.30 mg cm^{-2}. For comparison, 5.0 mg of commercially available Pt/C (20 wt%) was also dispersed on the GC electrode in the same way.

Before the ORR activity meas.ments, the electrolyte solution was degassed with high purity oxygen or nitrogen at least 30 min. All CV curves were conducted at a scan rate of 50 mV s^{-1} and LSV curves were meas.d with 5 mV s^{-1} in 0.1 M KOH. The diffusion-limited current density (J_L) was recorded at 0.2 V vs. RHE. The effective active surface areas (ECSA) of the electrocatalysts were collected by measuring the CV curves at different scan rates (40-140 mV s^{-1}) in order to estimate the degree of exposed electrochemically active sites on the working electrode. The stability of the active materials was conducted in O_2-saturated 0.1 M KOH solution at 1600 rpm *via* i-t (current *versus* time) curve. Electrochemical impedance spectra (EIS) meas.ments have been studied under an open-circuit potential (OCP) over a frequency range of 0.1-10^5 Hz and amplitude applied voltage of 5 mV. Methanol tolerance tests were carried out by chronoamperometry meas.ments in the case of injecting the 3.0 M methanol into the electrolyte. The accelerated durability test was conducted in O_2-saturated 0.1 M KOH solution at a scan rate of 100 mV s^{-1} with the potential between 0.6 V and 1.0 V (vs.RHE) for 10000 cycles.

1.4 Zinc-air /iodide hybrid batteries:

The meas.ments of zinc-air batteries were evaluated under ambient conditions. A polished zinc plate and 6.0 M KOH + 3 M KI solution were used as anode and electrolyte, respectively. The cathode was prepared by loading S-CNT@PFePc or Pt/C catalysts on the carbon paper (catalyst loading amount of 1.0 mg cm^{-2}).

1.5 Flexible solid-state Zinc-air /iodide hybrid batteries:

In a typical assembly for the solid-state Zinc-air battery, a polished Zn foil (1 × 3 cm^2, with another 1 × 3 cm^2 left blank as current collector) was employed as the anode, catalysts coated on carbon cloth (1 × 3 cm^2, with another 1 × 3 cm^2 left blank as current collector) were pressed to top of gel polymer as the cathode, then two pieces of white breathable tapes were used to seal the device. As for the catalyst inks, we prepared by blending 5 mg of the S-CNT@PFePc catalyst with 800 μL ethanol and 30 μL Nafion solution (5 wt%) by sonication for 30 min. As a contrast, 5 mg of commercial precious metal catalysts (Pt/C: RuO_2 = 1: 1, molar tatio) and 30 μL of 5 wt% Nafion solution were dispersed in 800 μL ethanol with sonication for 30 min. The gel polymer electrolyte was prepared briefly as follow: polyvinyl alcohol (4 g) powder was dissolved into 40 ml deionized water at 95 °C under stirring until the solution became homogeneous and transparent. Then, 4 mL of 18 M KOH+3 M KI was added dropwise for another 40 min at 95 °C under stirring. After that, the solution was po.d onto a mould and freezed in a freezer at -20 °C for 2 h with 0 °C for 4 h. Then, Add 4g of KOH dissolved in 4 mL of water while hot into the PVA solution to finally obtain a PVA solution containing approximately 1.6 M KOH. Continue stirring for 40 minutes. After that, the solution was po.d onto a mould and freezed in a freezer at -20 °C for 2 h with 0 °C for 4 h.

1.6 DFT calculation:

All calculations were performed by spin-polarized density functional theory (DFT) as implemented in Material Studio 2020. Generalized gradient approximation (GGA) with Perdew-Burke-Ernzerhof (PBE) exchange correlation functional was employed to described the valence electrons. The projector augmented wave function (PAW) is approximately the core electrons. In all calculations, the cut off energy was set to 500 eV. The geometry was optimized until the energy was converged to 1.0 × 10^{-6} eV $atom^{-1}$ and the force was converged to 0.05 eV $Å^{-1}$. The integration

of the Brillouin zone was sampled by a 4 × 4 × 4 γ mesh for S-CNT@PFePc, N-CNT@PFePc and CNT@PFePc models.

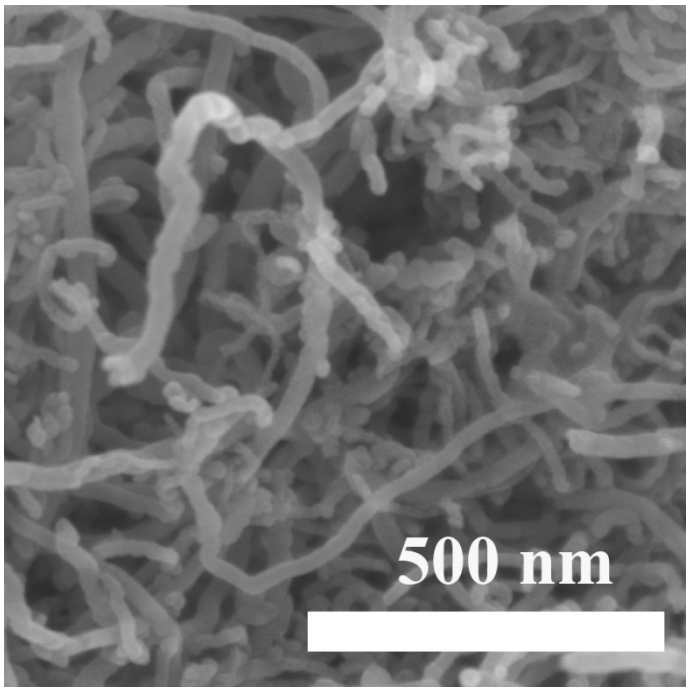

Fig. S1. SEM image of S-CNT.

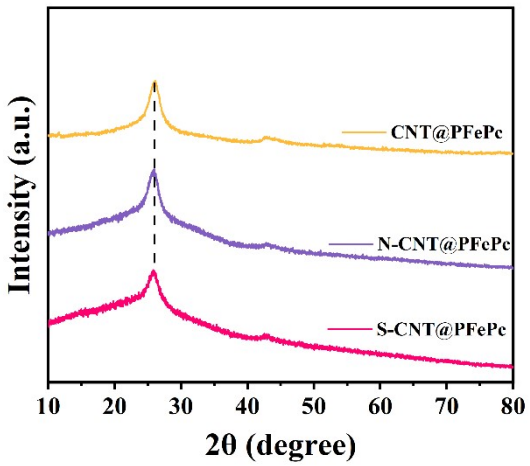

Fig. S2. XRD patterns of CNT@PFePc, N-CNT@PFePc and S-CNT@PFePc.

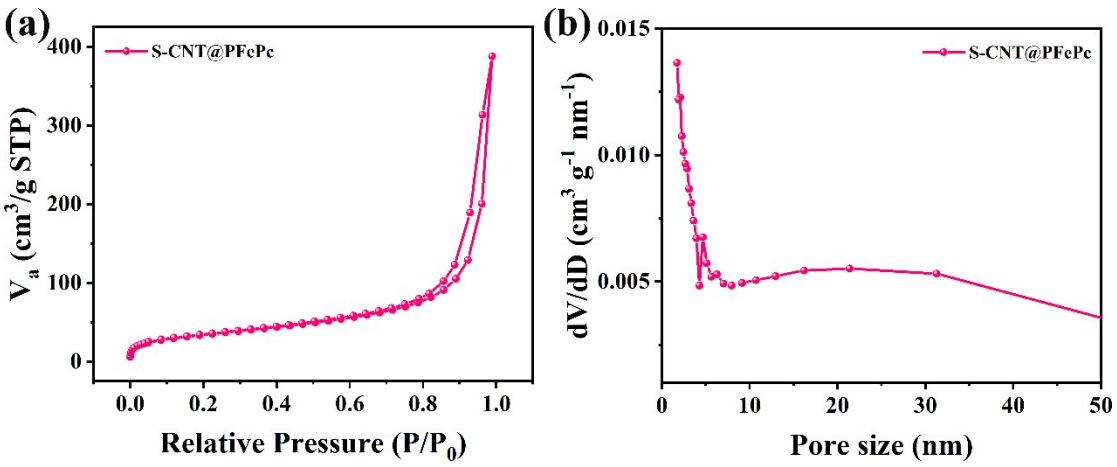

Fig. S3. (a) Nitrogen adsorption/desorption curves of S-CNT@PFePc; (b) Pore size distributions of S-CNT@PFePc.

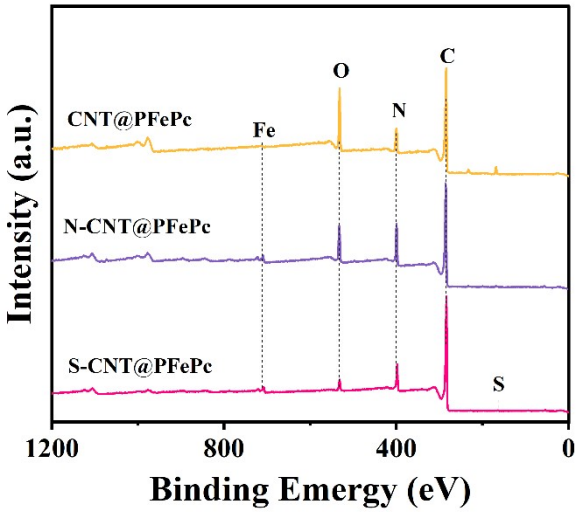

Fig. S4. XPS full spectra of CNT@PFePc, N-CNT@PFePc, and S-CNT@PFePc.

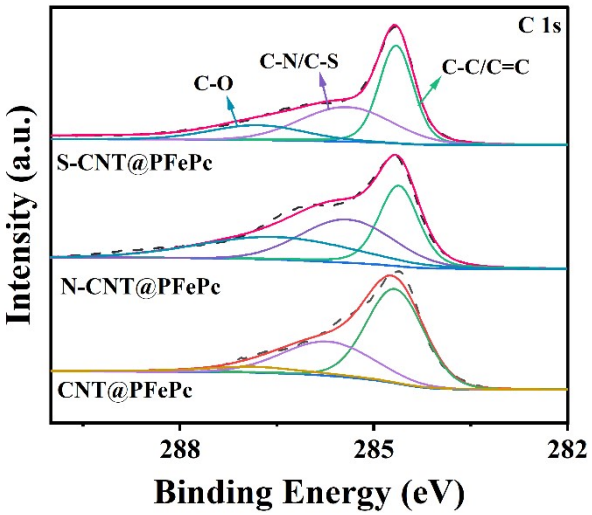

Fig. S5. XPS spectra of C 1s of the CNT@PFePc, N-CNT@PFePc, and S-CNT@PFePc.

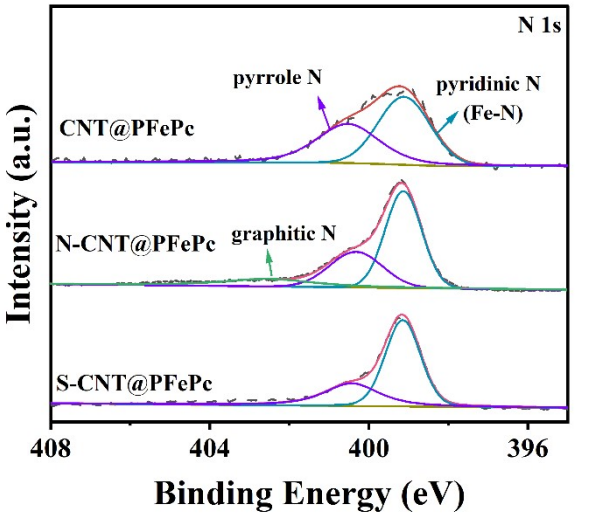

Fig. S6. XPS spectra of N 1s of the CNT@PFePc, N-CNT@PFePc, and S-CNT@PFePc.

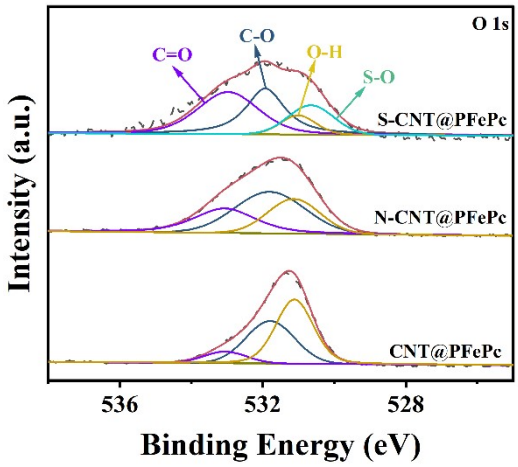

Fig. S7. XPS spectra of O 1s of the CNT@PFePc, N-CNT@PFePc, and S-CNT@PFePc.

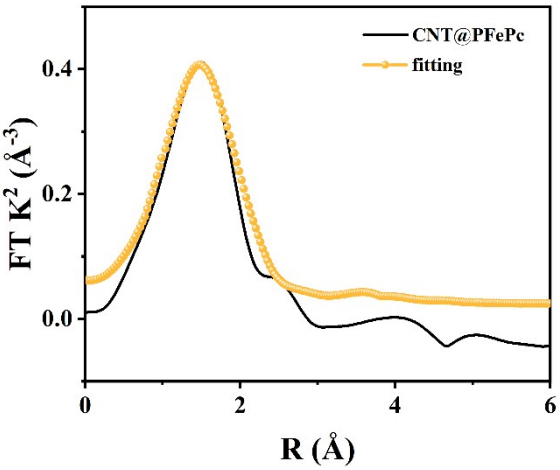

Fig. S8. The fitting curves of CNT@PFePc.

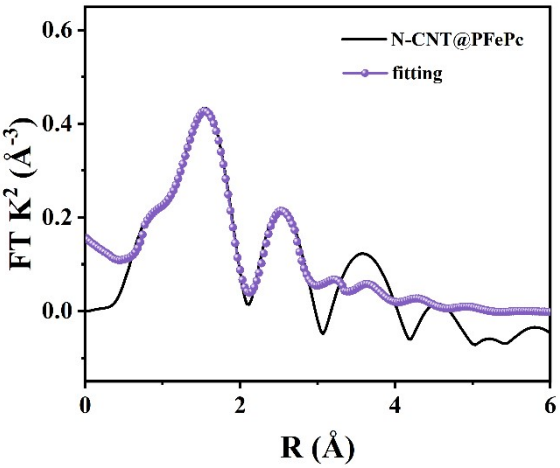

Fig. S9. The fitting curves of N-CNT@PFePc.

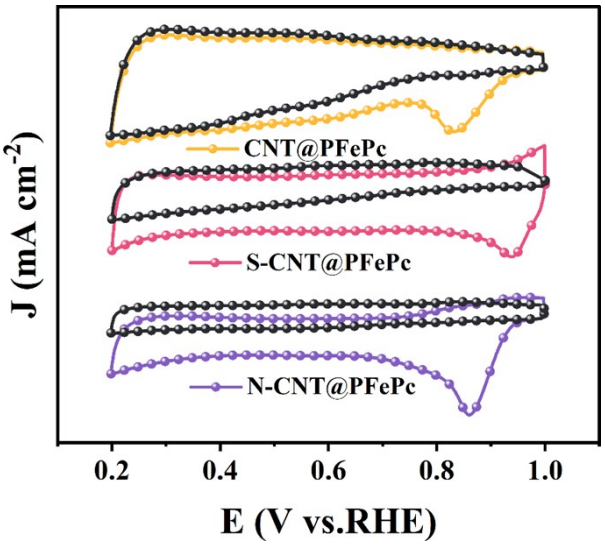

Fig. S10. Cyclic voltammetry tests for S-CNT@PFePc, N-CNT@PFePc and CNT@PFePc.

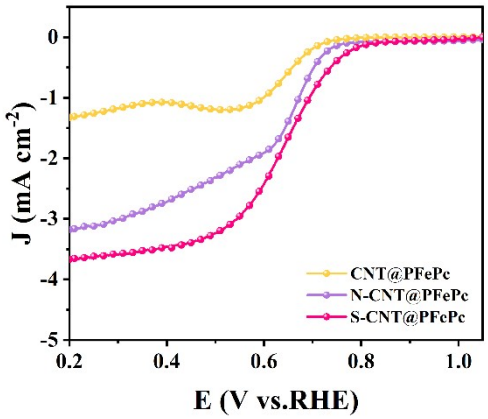

Fig. S11. ORR polarization curves tests for S-CNT@PFePc, N-CNT@PFePc and CNT@PFePc with 0.5 M KSCN+0.1 M KOH.

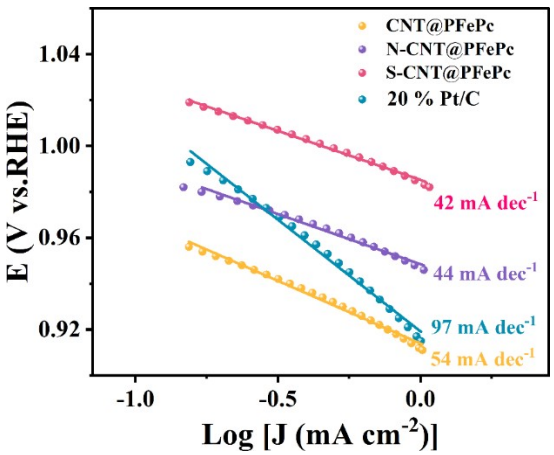

Fig. S12. Tafel slope for CNT@PFePc, N-CNT@PFePc and S-CNT@PFePc in 0.1 M KOH solution.

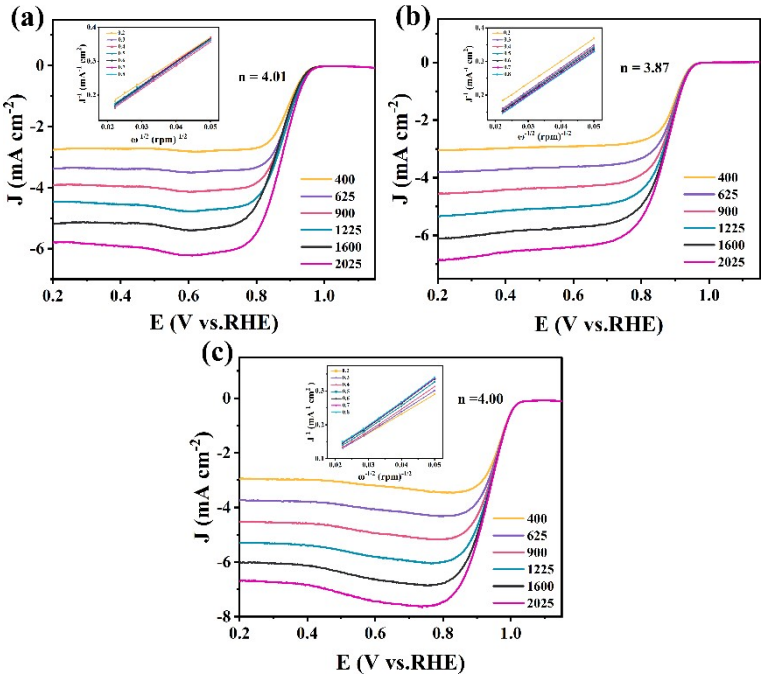

Fig. S13. Polarization curves and K-L plots of (a) CNT@PFePc and (b) N-CNT@PFePc, and (c) S-CNT@PFePc at different rotating speeds.

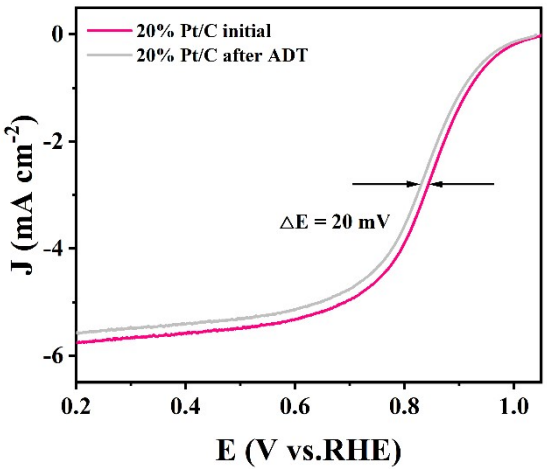

Fig. S14. LSV curves for 20% Pt/C catalysts initial and after accelerated durability tests.

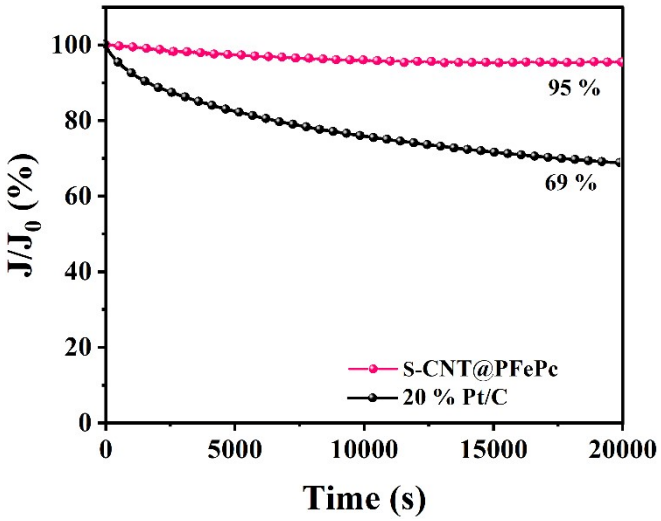

Fig. S15. i-t curves of stability for S-CNT@PFePc and 20% Pt/C.

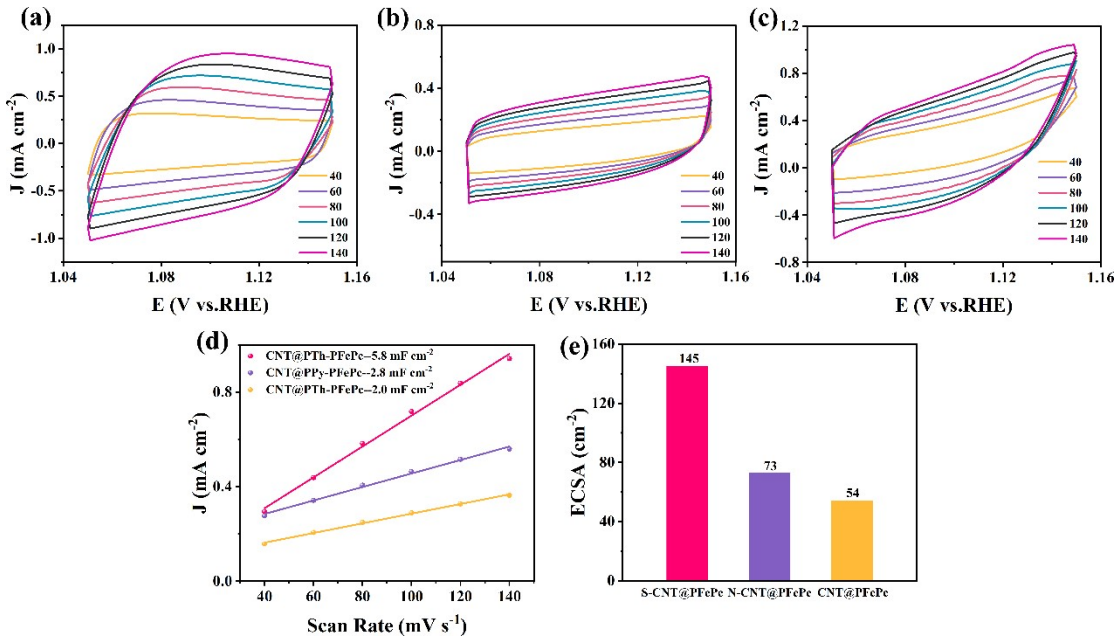

Fig. S16. Cyclic voltammograms (CV) at various scan rates of (a) CNT@PFePc, (b) N-CNT@PFePc, and (c) S-CNT@PFePc in 0.1 M KOH solution; (d) Plots of the capacitive currents as a function of scan rate for samples as well as the double-layer capacitance values for samples; (e) Plots of the ECSA values for samples. The ECSA can be calculated as: ECSA = C_{dl}/C_s. C_s is the specific capacitance value for a flat standard with 1 cm^2 of real surface area. The general value for C_s is between 20 μF/cm^2 and 60 μF/cm^2. Here we use 40 μF/cm^2 as the average value (*Nat. Commun.* **2015**, *6*, 8668).

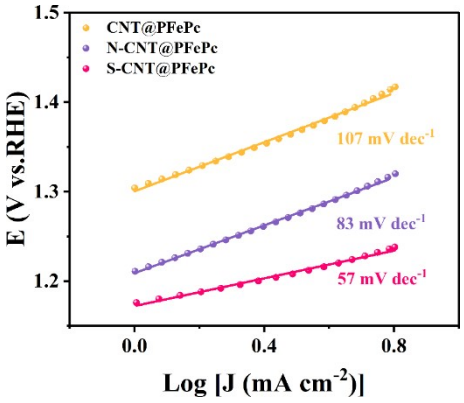

Figure S17. Tafel slope for CNT@PFePc, N-CNT@PFePc and S-CNT@PFePc in 1 M KOH+0.5 M KI solution.

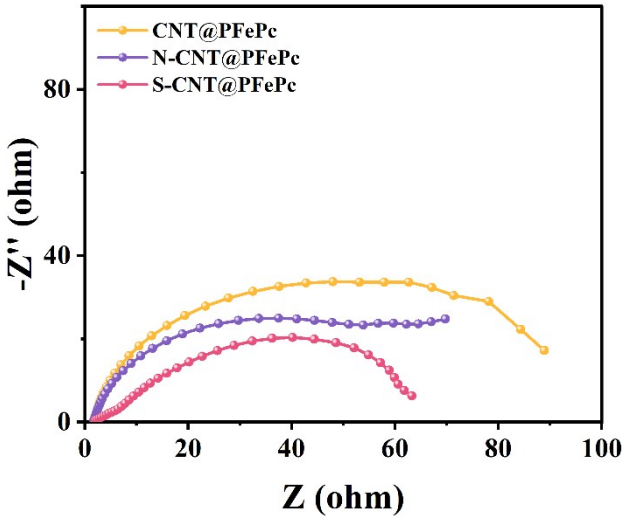

Fig. S18. Electrochemical impedance spectroscopy for CNT@PFePc, N-CNT@PFePc, and S-CNT@PFePc.

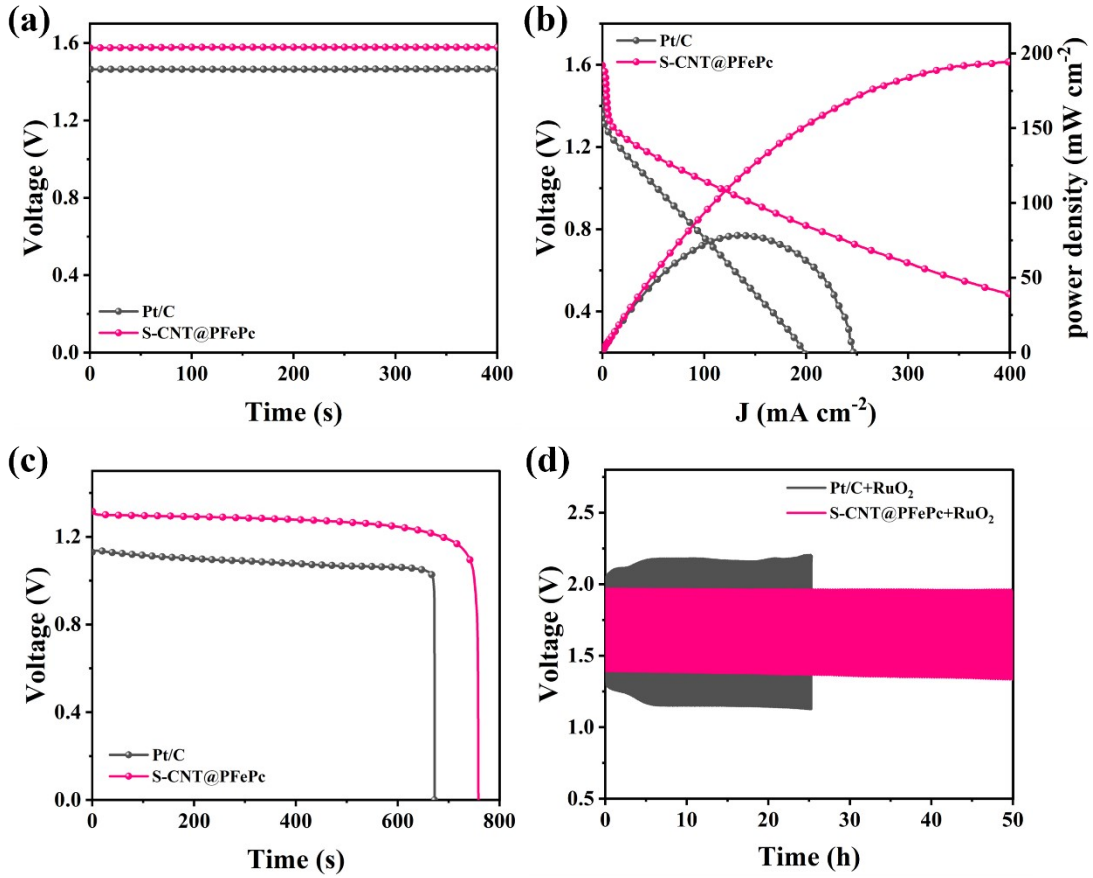

Fig. S19. a) Open circuit voltage curves; b) Power density curves; c) specific capacity d) Cycling performance of ZABs based the S-CNT@PFePc and Pt/C+RuO_2

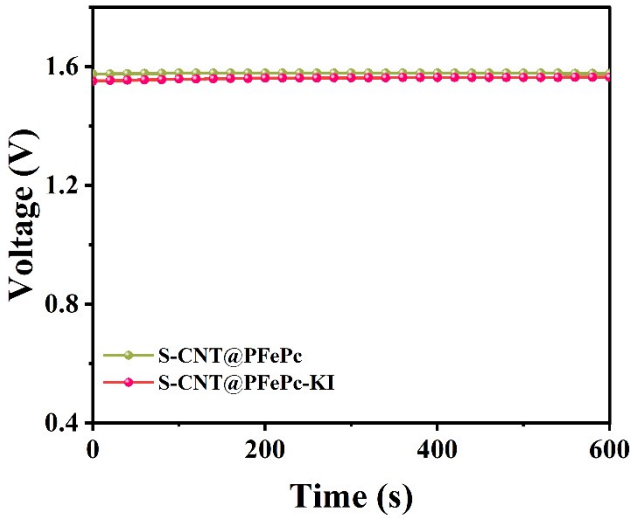

Fig. S20. Open-circuit voltage of S-CNT@PFePc -based ZAB and ZAIHBs.

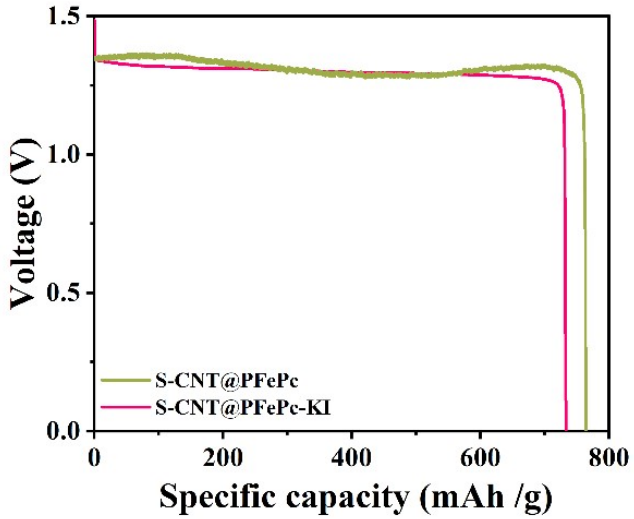

Fig. S21. Specific capacity of S-CNT@PFePc -based ZABs and ZAIHBs.

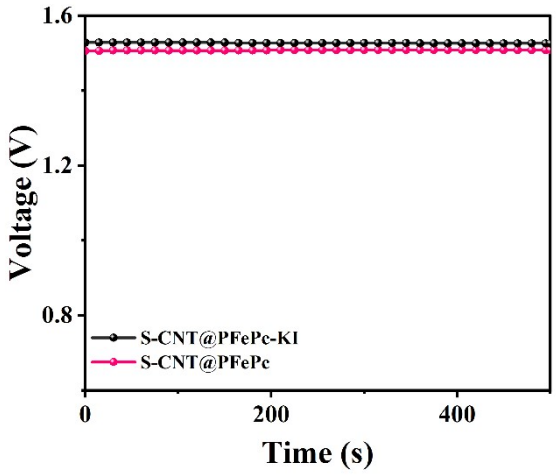

Fig. S22. Open-circuit voltage of S-CNT@PFePc -based flexible solid-state ZABs and ZAIHBs.

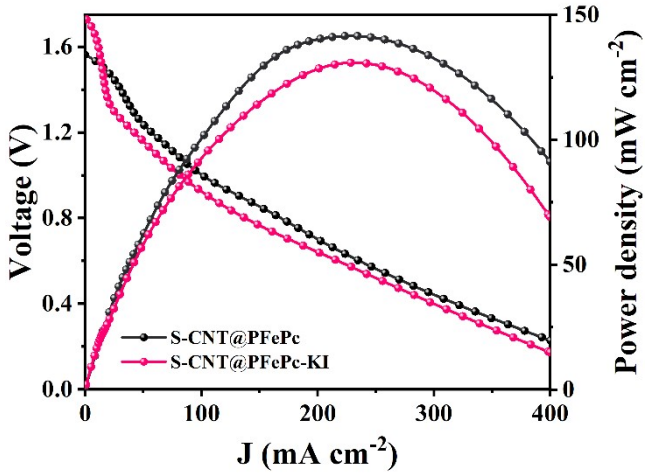

Fig. S23. Peak power density of S-CNT@PFePc -based flexible solid-state ZABs and ZAIHBs.

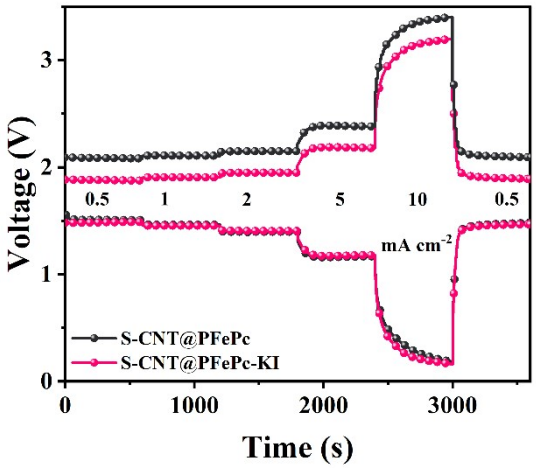

Fig. S24. Charge and discharge rate performances of S-CNT@PFePc -based flexible solid-state ZABs and ZAIHBs.

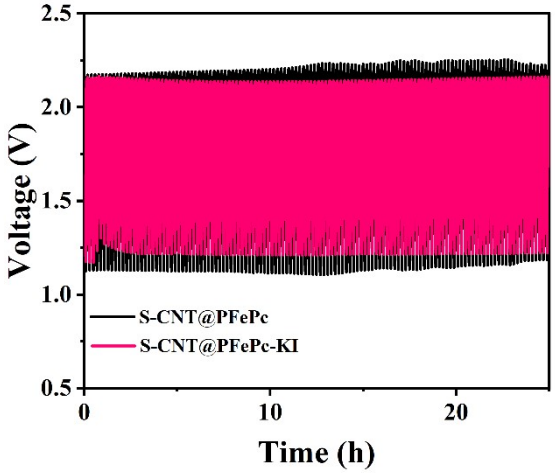

Fig. S25. Cycling performance of the zinc-air battery at a current density of 5 mA cm^{-2} of S-CNT@PFePc -based flexible solid-state ZABs and ZAIHBs.

Fig. S26. Open-circuit voltage of S-CNT@PFePc -based coin-type ZAIHBs.

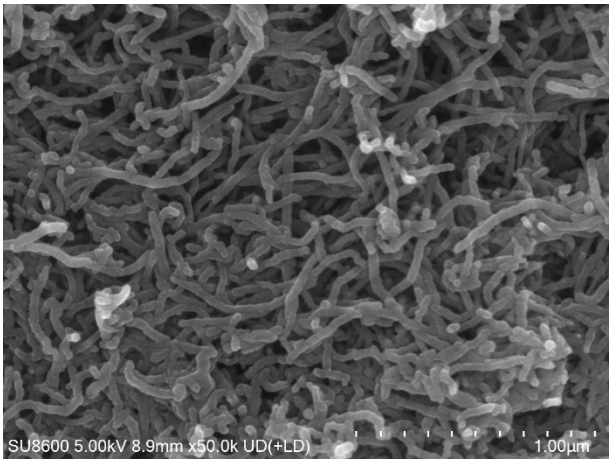

Fig. S27. SEM image of S-CNT@PFePc after ZAIHBs cycling.

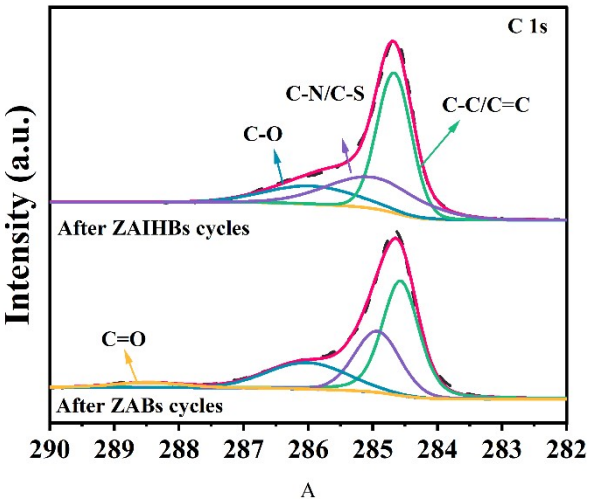

Fig. S28. The high-solution C 1s spectra of S-CNT@PFePc after cycles with and without KI.

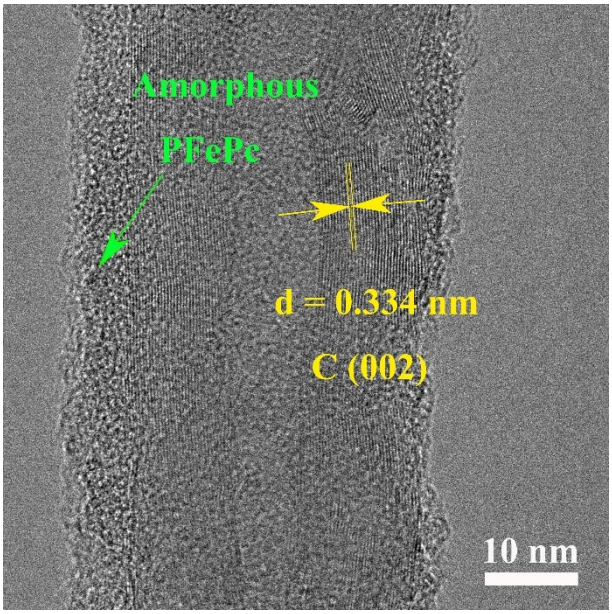

Fig. S29. The HRTEM image of S-CNT@PFePc after cycles with KI.

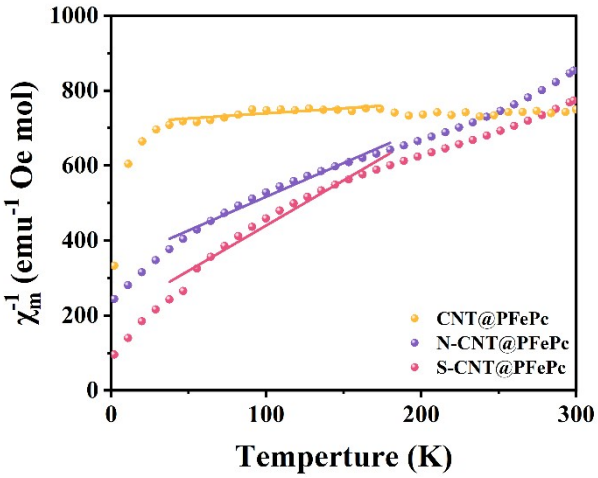

Fig. S30. The Curie−Weiss fitting results for S-CNT@PFePc, N-CNT@PFePc, and CNT@PFePc.

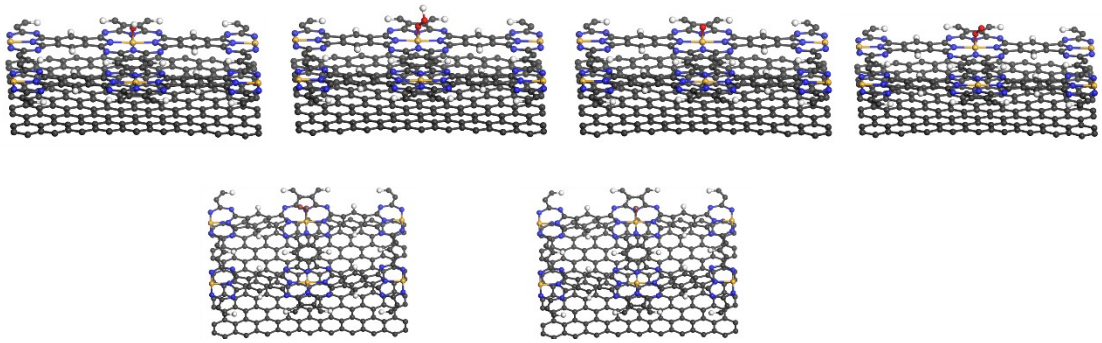

Fig. S31. Configurations of adsorbates on CNT@PFePc.

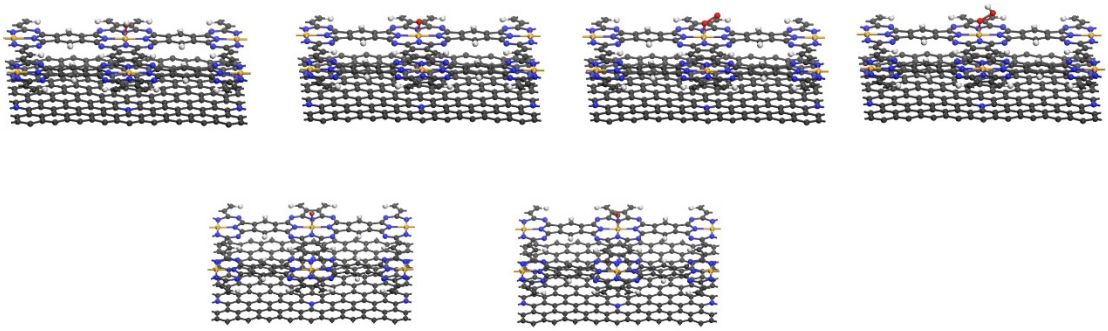

Fig. S32. Configurations of adsorbates on N-CNT@PFePc.

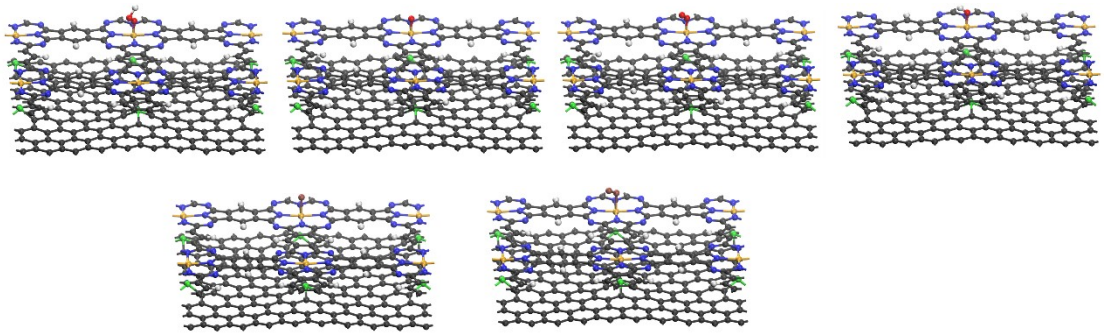

Fig. S33. Configurations of adsorbates on S-CNT@PFePc.

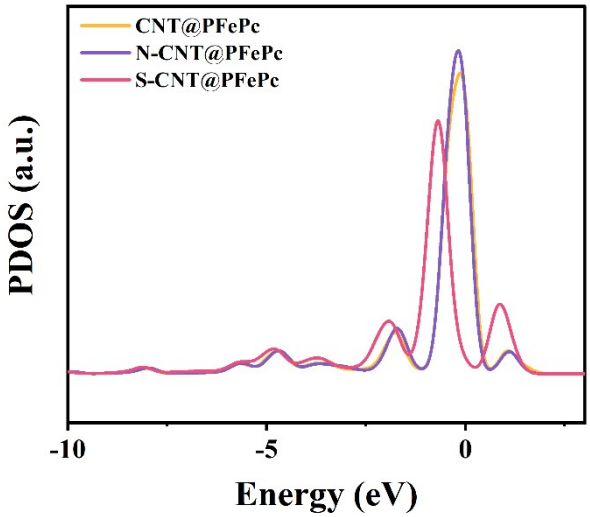

Fig. S34. The PDOS for S-CNT@PFePc, N-CNT@PFePc, and CNT@PFePc.

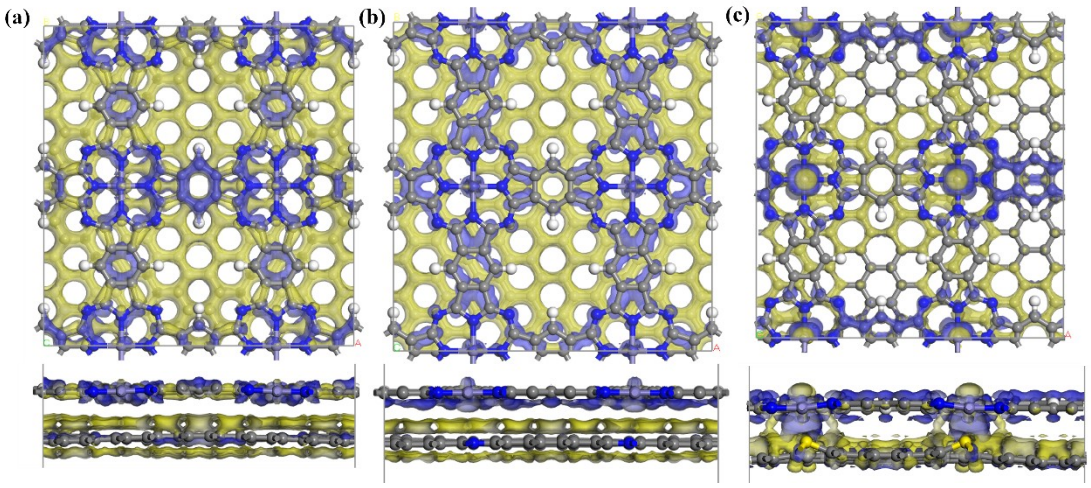

Fig. S35. The charge density difference plot of a) CNT@PFePc, b) N-CNT@PFePc and c) S-CNT@PFePc (blue represent electrons accumulation and yellow represent electrons depletion).

CNT@PFePc	N-CNT@PFePc	S-CNT@PFePc
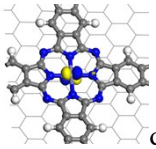 d_{xz}=-4.49	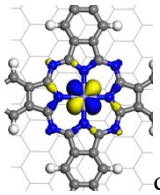 d_{xy}=-5.81	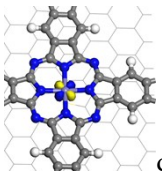 d_{xy}=-5.73
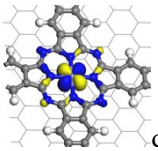 d_{xy}=-4.67	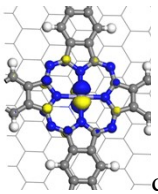 d_{yz}=-5.05	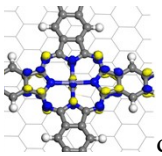 d_{yz}=-4.98
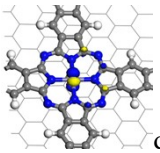 d_{yz}=-4.49	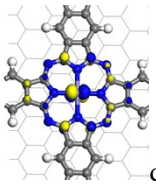 d_{xz}=-4.98	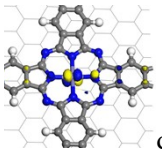 d_{xz}=-4.91
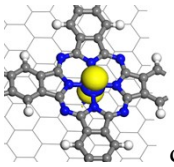 d_{z^2}=-4.34	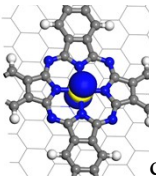 d_{z^2}=-3.81	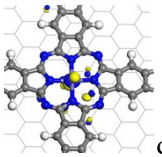 d_{z^2}=-4.02
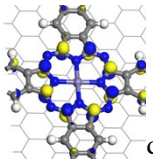 $d_{x^2-y^2}$=-3.02	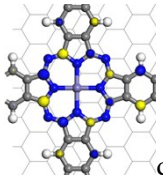 $d_{x^2-y^2}$=-3.33	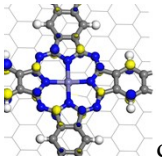 $d_{x^2-y^2}$=-3.48

Fig. S36. Natural localied molecular orbitals graphs and the corresponding energy level of the Fe 3d orbitals considering interations between ligands and Fe centers in S-CNT@PFePc, N-CNT@PFePc, and CNT@PFePc.

Table S1. The element content of XPS analysis in S-CNT@PFePc, N-CNT@PFePc, and CNT@PFePc.

Samples	C Content %	O Content / %	N Content / %	Fe Content / %	S Content/ %
CNT@PFePc	83.04	3.81	12.12	1.03	0
N-CNT@PFePc	81.99	1.17	15.63	1.21	0
S-CNT@PFePc	82.43	3.77	12.5	0.91	0.39

Table S2. Parameters of the Fe K-edge EXAFS fitting results for S-CNT@PFePc, N-CNT@PFePc, and CNT@PFePc.

Catalyst	Path	CN	R(Å)	σ^2 (10^{-3}Å^2)	ΔE_0	R-factor (%)
S-CNT@PFePc	Fe-N	5.0±0.2	1.85	0.0123	1.18	0.0103
	Fe-S	1.0±0.1				
N-CNT@PFePc	Fe-N	5.1±0.1	1.84	0.0033	1.03	0.0027
CNT@PFePc	Fe-N	3.9±0.1	1.75	0.0093	0.95	0.0083

Table S3. Comparison of the ORR performance for S-CNT@PFePc and others in 0.1 M KOH.

Catalyst	E_{onset}/V	$E_{1/2}$/V	Reference
S-CNT@PFePc	1.03	0.94	This Work
Cu, Fe/NC	0.98	0.89	Chem. Eng. J. 2025, 507, 160400.
CMNCA-Fe_{SA+AC}	0.99	0.91	Small 2025, 21, 2500419.
NiFe-N-C	0.96	0.87	Energy Environ. Sci., 2024, 17, 704.
FePNC	0.99	0.88	Adv. Energy Mater. 2023, 13, 2301223.
FePc/GDYO	0.96	0.89	Chem. Eng. J. 2025, 510, 161001.
FePc/Eu_2O_3	1.00	0.93	Adv. Funct. Mater. 2025, 2425138.
FeN_5	0.99	0.85	Small 2023,19, e2300373.
Fe–N,O/G	1.01	0.86	Energy Environ. Sci. 2023,16, 2629-2636.
SA-FeN_5/HPC	1.03	0.93	Small 2025, 21, 2500897
Zn/Fe-NC	0.95	0.79	Angew. Chem. Int. Ed. 2025, e202501531.
FeSA-Fe_3C/NC	1.01	0.90	Angew. Chem. Int. Ed. 2025, 64, e202501266.
FeSA-CoNP@NC-2		0.90	Chem. Eng. J. 2025, 511, 162281.

Table S4. Comparison of the voltage gaps between ORR and OER (or UOR, or IOR) for S-CNT@PFePc and others.

Catalyst	$E_{1/2}$/V	$E_{j=10}$/V	ΔE/V	Reference
S-CNT@PFePc	0.94	1.28	0.34	This Work
Fe–N–C/Fe_3C-op	0.91	1.58	0.67	Adv.Sci. „2301656.
Co_3O_4/rmGO	0.79	1.62	0.83	Science. 2009, 323, 760.
CNT/graphenehybrid	0.76	1.51	0.75	Nat.Mater. 2011, 10, 780.
NCNTFs	0.87	1.6	0.73	Nat. Nanotechnol. 2012, 7, 394.
SCCoO	0.85	1.56	0.71	Nat.Energy 2016, 1, 15006.
$MnCo_2O_4$	0.85	1.63	0.78	Nat. Commun. 2016, 7, 12876.
$Nd_{1.5}Ba_{1.5}CoFeM_nO_{9-\sigma}$	0.698	1.589	0.891	Angew. Chem., Int. Ed. 2017, 56, 14977.
PdMobimetallene	0.95	1.7	0.75	Sci. Adv. 2018, 4, eaap9360.
$(Co,Fe)_3N$	0.81	1.62	0.81	Nat. 2019, 574, 81..
MoS_2@Fe–N–CNSs	0.84	1.7	0.86	Nat. Commun. 2020, 11, 1952.
Fe,Mn/N-C	0.93	1.62	0.59	Nat.Commun. 2021, 12, 1734.
CoNCSAC	0.86	1.65	0.79	J. Am. Chem. Soc. 2022, 144, 4783.
FeMn-DSAC	0.92	1.64	0.72	Angew. Chem., Int. Ed. 2022, 61, e202115219.
Ni_3S_2/Co_9S_8@Co-NC	0.85	1.49	0.64	J. Mater. Chem. A,2025, 13, 9974.
NiFeVS	0.79	1.59	0.80	Adv. Funct. Mater., 2024, 34, 2310181
CoNP@FeNC-0.05	0.85	1.63	0.78	Nano Micro Lett., 2023, 15, 26.
$Fe_8Co_{0.2}$-NC-800	0.82	1.63	0.81	Nano Micro Lett., 2023, 15, 26.
NCMS/NrGO	0.83	1.59	0.75	J. Mater. Chem. A, 2024, 12, 11945-11959.
CoNi/Co–NCNT	0.87	1.43	0.56	J Materiomics 2025, 11, 100965.

Ni SAs-NC	0.85	1.39	0.54	Appl. Catal. B Environ. 2022, 310, 121352.
N–HCS@NiFe	0.80	1.35	0.55	Green Chem., 2024, 26, 12043.
$Co/CoSe_2@CN_x$	0.83	1.34	0.51	J. Mater. Chem. A 2023, 11, 5179.
CoNi@NCNTsLDH/CC	0.84	1.36	0.52	Appl. Catal. B Environ. 2024, 354, 124115.
$Co_{5.47}$ N PCNFs	0.79	1.22	0.43	J. Colloid Interface Sci. 2025, 680 469–478.
nh-W/N/C	0.91	1.36	0.45	Electrochim. Acta 2024, 475 143587.

Table S5. Performance comparison of rechargeable Zn-air batteries using non-noble metal.

Number	Catalysts	Power density (mW cm^{-2})	Energy efficiency	Cycling stability	Refs.
	S-CNT@PFePc	197	70%	500	This work
1	$Co/CoSe_2@CN_x$	113	62.1%	140	J. Mater. Chem. A 2023, 11, 51795187
2	Ni SAs-NC	172	71.8%	300	Appl. Catal. B Environ. 2022, 310,121352
3	Co1Fe1-N-C	100	68%	230	Small 2023, 2307863
4	$Pt/C-Co_3O_4$	78.6	73%	200	Adv. Mater. 2020, 32, 1908127
5	pfSAC-Fe-0.2	123.4	62%	300	Sci. Adv. 2019, 5 eaaw2322
6	Sn-N/O-C	254	58.3%	220	Adv. Energy Mater. 2024, 2303740
7	NCNF-1000	185	62 %	100	Adv. Mater. 2016, 28, 3000
8	$Fe_2Ni@NC$	126	62.1 %	300	Adv. Energy Mater. 2020, 10,1903003
9	Ce SAs/PSNC	212	52.2 %	325	Adv. Mater. 2023, 35, 2302485
10	Ni-NC	87.7	69.3 %	100	Mater. Today Phys. 2022, 29,100924
11	FeCo-N-C-hierarchical	129	66.9 %	250	Chin. Chem. Lett. 2023, 34,107807.
12	Fe/Co-N/S-Cs	102.6	66.7 %	26.7	Appl. Catal., B 2019, 241, 95.
13	Sb-SeNC	54	60.9 %	400	ACS Catal. 2023, 13, 7122-7131.
14	Fe2N6-S	200	55 %	400	Adv. Mater. 2024, 2309231.
15	NiFe-LDH/Fe1-N-C	205	62 %	400	Adv. Energy Mater. 2023, 13,2203609.
16	Cu-N4/Fe2-N6	156	61.5 %	400	Energy Environ. Sci. 2023, 16, 3576.